Chemical Engineering Journal 108 (2005) 69–79

Chemical Engineering Journal

www.elsevier.com/locate/cej

Studies on hydrodynamics of an internal-loop airlift reactor in gas entrainment regime by particle image analyzer

Tsao-Jen Lin*, Po-Chou Chen

Department of Chemical Engineering, National Chung-Cheng University, Chia-Yi 621, Taiwan

Received 28 April 2004; received in revised form 16 December 2004; accepted 3 January 2005

Abstract

Experiments conducted quantify the hydrodynamic characteristics of a two-dimensional (2D) internal-loop airlift reactor in a gas entrainment regime, which is divided into two sub-regimes differentiated by re-circulating bubbles back to the riser (i.e., Regimes I and II). Both flow visualization and full-field measurements using particle image analyzer (PIA) have been performed. Contours for instantaneous vorticity, averaged velocity, and Reynolds stresses are obtained and discussed in relation to measurable coherent structures present in the flow. In Regime I, the riser comprises four coherent structures, including the descending, vortical, fast bubble and central plume flows. Due to reducing the local density by trapping small bubbles in the vortical flow along with recycling a small portion of liquid back to the riser, the flow conditions exhibit a weaker vortical flow, less significant changes in both normal and shear stresses, and the inversion point shifts to a location 90% diameter of the riser. For Regime II, the central fast bubble flow results in a parabolic profile of the vertical velocity with a maximal value at center and an inverse point at 70% diameter of the riser. The maximal values of the normal stresses, $\langle U'U' \rangle$ and $\langle V'V' \rangle$, are located at the centre of the riser and are induced by the swing of the fast bubble flow and close to the sidewall provoked by the vertical fluctuation of the vortical flow, respectively.

Keywords: Internal-loop airlift reactor; Hydrodynamics; Multiphase flow; Visualization; Particle image analyzer

1. Introduction

Airlift reactors have been widely applied in many biotechnological and chemical processes [1–3]. The advantages of airlift reactors provide efficient mixing, avoiding destruction in shear sensitive organisms, and requiring low energy input and simple construction [4–6]. The intrinsic complicated hydrodynamic structures induced by bubble motion and associated with wake interaction, have been recognized to be the key factors responsible for heat and mass transfers. Because bubble-induced flows in the airlift reactor are identified to be dynamic in nature, the time averaged flow properties cannot well represent the dynamic governing mechanisms of flow structures. Hence, it is apparent that the quantification of the instantaneous, rather than time- or volume-averaged, hydrodynamic flow phenomena is required to provide further insight into the design and scale-up of airlift reactors [7–10].

Based on the configuration of the geometry, airlift reactors are generally classified into two main categories: internal-loop and external-loop [11]. In fact, an airlift reactor is a modified bubble column reactor. The riser section of an airlift reactor can be regarded as a bubble column. On account of the additional loop for liquid circulation, fluid dynamic conditions are altered and cause the operation range of the airlift reactor to be different from that of the bubble column [12,13]. Normally, an airlift reactor can be operated at higher liquid circulating velocities and larger gas throughputs without formation of slugs. Liquid circulation is caused by the hydrostatic pressure difference between riser and downcomer and by the ascending bubbles which drift the liquid upward. When the liquid circulation velocity is sufficient, the gas bubble will be carried over into the downcomer and

* Corresponding author. Tel.: +886 5 2720411x33405; fax: +886 5 2721206.
E-mail address: chmtjl@ccu.edu.tw (T.-J. Lin).

1385-8947/$ – see front matter © 2005 Elsevier B.V. All rights reserved.
doi:10.1016/j.cej.2005.01.001

Nomenclature

N	the total number of vectors in the strip
U	liquid velocity component in radial direction (cm/s)
$\langle U \rangle$	time-averaged radial velocity (cm/s)
U_b	bubble velocity component in radial direction (cm/s)
U_g	superficial gas velocity (cm/s)
$\langle U'U' \rangle$	radial normal stress (cm^2/s^2)
$\langle U'V' \rangle$	shear stress (cm^2/s^2)
V	liquid velocity component in axial direction (cm/s)
V_b	bubble velocity component in axial direction (cm/s)
$\langle V \rangle$	time-averaged axial velocity (cm/s)
$\langle V'V' \rangle$	axial normal stress (cm^2/s^2)

Greek symbol

Δx	interrogation grid interval in the radial direction (cm)
Δy	interrogation grid interval in the axial direction (cm)
ω	vorticity component of liquid phase in the z direction (s^{-1})

from the downcomer into the riser again. Hence, from the viewpoint of bubble entrainment into the downcomer, three gas flow regimes are commonly distinguished with increasing gas velocities: no gas entrainment, gas entrainment but no gas re-circulation, and complete gas re-circulation [14,15]. Meanwhile, corresponding to the above flow regimes, three different flow structures can also be identified in the riser: the dispersed bubble, churn-turbulent, and slugging [12].

In the past, few studies on the hydrodynamics of airlift reactors have been undertaken by experimental and theoretical analyses. The experimental investigations can be classified into two approaches—global and local measurements. First, in the global measurements, a number of correlations have been developed to estimate gas hold-up and liquid circulation velocity of airlift reactors [16–19]. These presented empirical correlations which have limitations and cannot be generalized to all operation and design variables. For theoretical analysis of global hydrodynamics, two main simplified models have been developed to estimate the mean liquid velocity and gas hold-up. One is a combination of macroscopic momentum or energy balance with empirical gas hold-up and friction factors [15,20]; and the other is a drift flux model incorporated with mechanical energy balance [21,22]. As for the local measurements, previous studies have mostly involved measurement of time/volume-averaged flow properties with the assumption that the flow is steady [23–25]. For example, Young et al. [23] and Utiger et al. [25] used hot-film anemometry and probe techniques, respectively, to measure the radial and axial velocity profiles of both phases as well as the gas hold-up in an external loop airlift reactor.

Although extensive efforts have been made to unveil the flow structure in the airlift reactor, a fundamental understanding, especially in the quantitative aspect, of the hydrodynamics is still inadequate. Limited by the measuring techniques and the complicated mechanisms of the systems, no quantitative instantaneous flow information for a whole flow plane can presently be obtained through the use of traditional, both intrusive and non-intrusive, measurement techniques. Applying laser Doppler anemometry (LDA) and probe techniques, Becker et al. [24] measured local hydrodynamics characteristics (e.g., turbulence intensity) of a flat rectangular loop reactor. However, this technique essentially gives point information. Recently, particle image velocimetry (PIV), providing a quantitative means for measuring the instantaneous flow field of a plane, overcame these measurement limitations. The PIV system is a non-intrusive technique that allows for the measurement of full-field flow information by utilizing advanced image acquisition and computer processing technique [26–28]. By this technique, Lin et al. [27] have reported quantitative assessments of the macroscopic flow structures under different scale two-dimensional (2D) bubble columns. Also, Mudde et al. [28] performed a more complete analysis of microscopic phenomena by measuring the average Reynolds stresses and velocity profiles on the coherent structures in a 2D bubble column.

Chen and Chou [29] developed a new particle image analyzer system by improving the image processing techniques and adding some hydrodynamic calculations into the original PIV system. It has been reported that two- and three-dimensional (3D) systems can generate similar and compatible quantitative flow information of gas bubble dynamics in liquid and liquid–solid suspensions [30,31]. Meanwhile, Chen et al. [32] found that the flow structures in 2D and 3D bubble columns are similar through the qualitative flow visualization. They found that the wavelike motion of the fast bubble flow in 2D bubble columns becomes a spiral motion in 3D bubble columns. Although there are limitations in similarity between 2D and 3D systems, the structures present in the flow field in 2D systems can qualitatively enlighten a better understanding of those in 3D systems.

2. Experimental set-up

Fig. 1 shows the experimental apparatus. The apparatus includes a 2D internal-loop airlift reactor made of transparent Plexiglas sheets. The reactor is 32 cm in width, 1.2 cm in depth, and 100 cm in height. The riser (internal-loop) made of two movable vertical partitions allows the width to be varied. In this study, the riser is 17.5 cm in width and 54 cm in length, respectively, and is located 6 cm above the bottom of the reactor. The gas distributor is made up of six-tube injectors flush mounted on the bed wall at the entrance of

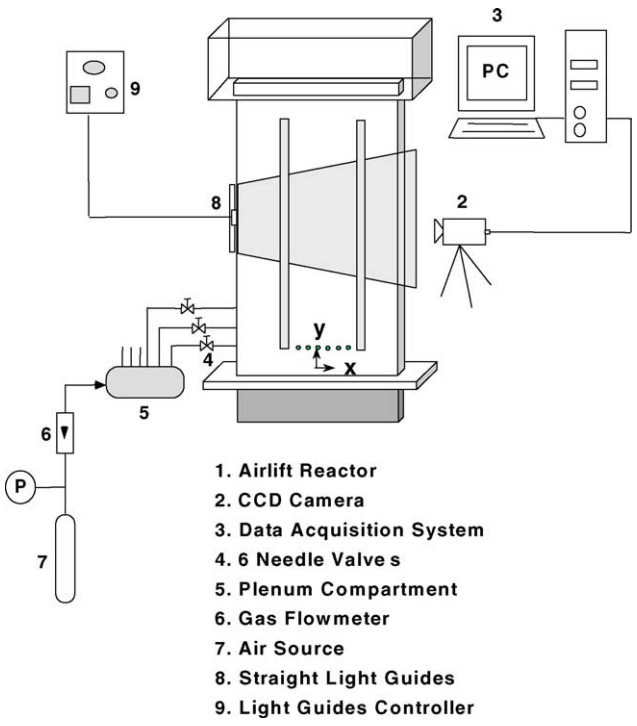

Fig. 1. Schematic diagram of the test facility.

the riser. The distance between two adjacent bubble injectors is 2.5 cm. Each gas injector opening is 0.16 cm-i.d. The gas flow through each injector is individually regulated by a needle valve connected to the plenum compartment outside of the bed. Tap water is used as the liquid phase and is operated under batch conditions. The static height is kept constant at 66 cm for the tests in this study. Neutrally buoyant Pliolite particles of size ≈250 μm and density ≈1.02 g/cm^3 are used as liquid seeding particles, and have a Stokes responding time around 7.0×10^{-3} s, which is much smaller than the time scale of the energy-containing eddies. To ensure that the seeding particles follow the flow closely and have virtually no effects on the flow structure, the concentration of the seeding particles is maintained around 1%. According to Einstein's law, the viscosity correction for 1% seeding particle is less than 2%, so the effect of the seeding particle on viscosity can be neglected. Note that the right hand side of the column is always investigated.

Through the sidewall, a light sheet 18 cm long is generated from a straight light guide. Connected with an optical fiber to the straight light guide, a 150 W halogen light source generator with a special filter lens provides a cold light to illuminate the flow field without raising the system temperature. The flow field is visualized and recorded by a video camera. A high speed and high-resolution CCD camera equipped with variable electronic shutters ranging from 1/60 to 1/8000 s is used to record the image of the flow field in the computer. A non-intrusive technique, PIA developed by Chen and Chou [29], is applied to measure the flow field. The technique of PIA discriminates between seeding particles and bubbles based on the size of the recorded images of the objects. There are five steps for the image processing, including image acquisition, image enhancement, particle identification and calculation of the centroids, discrimination of the particle images between the two phases, and matching of the particles in three consecutive video fields and calculation of the velocity of the identified triplets. The vectors obtained are located at the position of the centroid of the initial tracer particle in a triplet. Through the utilization of advanced image acquisition and computer processing techniques, the PIA system provides quantitative data on a flow plane including instantaneous velocity distributions, velocity fluctuations, and other statistical flow information. A commercially available program, TECPLOT, is utilized for post-processing the PIA data.

Considering the resolution of the seeding particles for image analysis, the image field of view is limited to 13.5 cm × 15.5 cm from the right half of the column. For each set test, three frames are combined to form a phase frame. The interval between two consecutive phases is 4 ms. The recorded flow field is divided into 34 × 36 grids to perform the interpolation, which results in a grid size of 0.397 cm × 0.43 cm. Execution of the interpolation process using the Kriging algorithm is performed for each phase frame. The *z*-component vorticities $\omega(i, j)$ of each grid point is calculated based on a finite-difference approximation for the interpolated velocity field as

$$\omega(i, j) \approx -\frac{\Delta U}{\Delta y} + \frac{\Delta V}{\Delta x} = -\frac{U(i, j+1) - U(i, j-1)}{2\Delta y} + \frac{V(i+1, j) - V(i-1, j)}{2\Delta x} \quad (1)$$

Here $U(i, j)$ and $V(i, j)$ are the velocity components in x and y directions at the interrogation grid point (i, j), correspondingly; Δx and Δy are the interrogation grid intervals in x and y directions, respectively. For the average quantities, profiles are calculated by dividing the field of view into vertical strips only. The vector $\{U(i, j), V(i, j)\}$ is attributed to a particular strip when the centroid of the initial tracer particle of a triplet is located in that strip. The average of the velocity components and the various Reynolds stresses for all fields for each strip are then calculated as specified in Eqs. (2)–(6) as given in Table 1.

3. Results and discussion

3.1. Description of flow structures

An example of the gas flow behaviors in the gas entrainment regime without gas re-circulation (Regime I), and with gas re-circulation (Regime II) back to the riser in a 2D internal-loop airlift reactor is shown in Fig. 2. When the gas velocity is operated between 0.7 and 2.2 cm/s, Regime I is encountered, as shown in Fig. 2(a). In this regime, the

Table 1
Equations of the averaged velocities and stresses

Averaged horizontal velocity	$(2)\langle U(i)\rangle = \frac{1}{N(i)} \sum_{\{x,y\} \in \text{strip}(i)} U(x, y)$	(2)
Averaged vertical velocity	$\langle V(i)\rangle = \frac{1}{N(i)} \sum_{\{x,y\} \in \text{strip}(i)} U(x, y)$	(3)
Horizontal normal stress	$\langle U'U'\rangle(i) = \left[\frac{1}{N(i)} \sum_{\{x,y\} \in \text{strip}(i)} U(x, y)U(x, y)\right] - (\langle U(i)\rangle)^2$	(4)
Vertical normal stress	$\langle V'V'\rangle(i) = \left[\frac{1}{N(i)} \sum_{\{x,y\} \in \text{strip}(i)} V(x, y)V(x, y)\right] - (\langle V(i)\rangle)^2$	(5)
Shear stress	$\langle U'V'\rangle(i) = \frac{1}{N(i)} \sum_{\{x,y\} \in \text{strip}(i)} [\{U(x, y) - \langle U(i)\rangle\}\{V(x, y) - \langle V(i)\rangle\}]$	(6)
	$N(i)$ is the total number of vectors in strip i	

recycled flow starts to entrain some small bubbles into the downcomer. The higher the gas velocity, the deeper and the larger bubbles are entrained but without being re-circulated back to the riser. Generally, the flow structure of the riser comprises a descending region, vortical region, fast bubble region, and central plume region. Clustered together by bubbles at the bottom, the fast bubble region moves in a wavelike manner. However, the coalescence is much less in the central plume region, and the bubble-bubble interactions are less significant. The flow condition is characterized by a gross circulation of the liquid phase, wherein the liquid rises in the middle portion of the column and largely passes into the downcomer.

Increasing the gas velocity over 2.2 cm/s, Regime II occurs, as shown in Fig. 2(b). In the riser, two fast bubble flow regions merge together to form one central fast bubble region in the center of the column without the central plume region. The gas flow in this regime is dominated by bubble coalescence and break-up. The vortical flow region and descending flow regions are still observable. A strong liquid flow, induced by wake effects from the large bubbles rising in the central part of the column, is circulated into the downcomer. This strong liquid flow drags a great number of bubbles all the way down to the downcomer and even back to the riser again. This produces the main difference in flow condition between Regimes I and II.

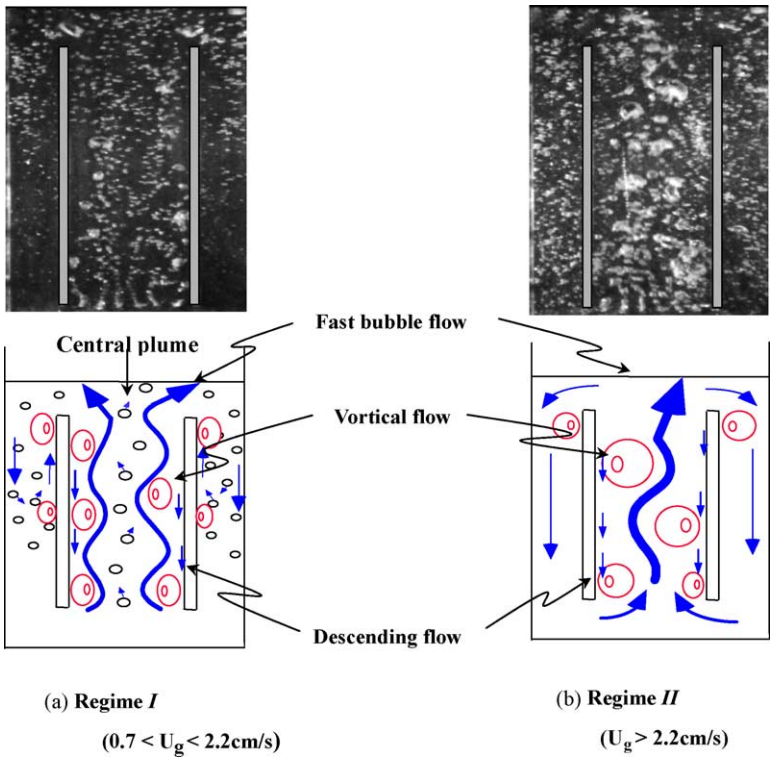

Fig. 2. Flow regimes and classification of regions in a two-dimensional internal- loop airlift reactor.

3.2. Instantaneous and time-averaged hydrodynamic analysis

For each operating regime under a specific gas velocity, the instantaneous and time-averaged flow structures have been quantitatively studied by using the PIA technique in the airlift reactor. The time-averaged data were obtained by analyzing at least 400 randomly grabbed pairs of frames, which were acquired within 10–15 min of the recorded images. To interpret the development of the flow structure, the reactor is divided into three sections, including bottom, middle, and upper sections, as shown in Fig. 3. The field of view is chosen at the right half of the column and the center of the riser is denoted as zero in the radial location. To ensure the validity of the analyses, a continuity check on a zero value for the summation of the average axial velocity is applied to all cases. Note that some of the streamlines in the figures issue from the boundary of the view that has little physical sense. This unreasonable result is apparently caused by the interpolation errors due to the lack of data in the vicinity of the view caused by tracers flowing out of the boundary. Nevertheless, the boundary regions are limited and should have little effect on the general interpretation of the flow structure.

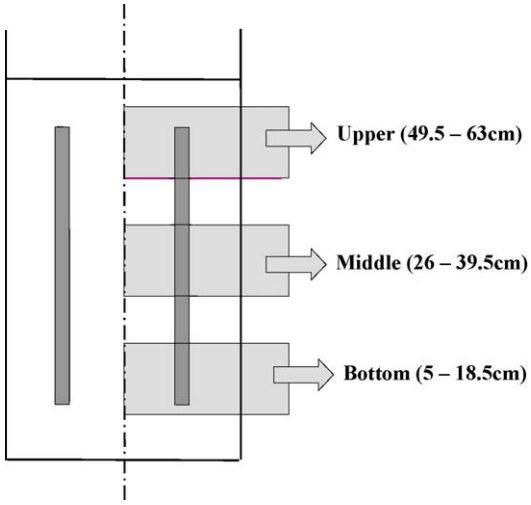

Fig. 3. The fields of view for the testing zones in the airlift reactor.

3.2.1. Regime I

The case is operated at $U_g = 1.43$ cm/s in Regime I, wherein the instantaneous flow images, streamlines and vorticity contours at three sections are shown in Fig. 4. As gas velocity increases, the strength of the circulated flow from the downcomer is enhanced and a stronger vortex is generated at the entrance of the riser. The bubbles in the central plume region remain at the dispersed bubbling status, but with larger bubble size. The bubble chains close to the sidewalls are suppressed by the vortex and migrate away to coalesce or cluster with adjacent bubble chains forming a fast bubble flow. As a result, the gas hold-up distribution in Fig. 5 shows a low value close to the sidewalls and a zigzag distribution outside the vortex. While moving upward, the fast bubble flow interacts with the descending liquid flow to generate the vortical flow. The generated vortical flow, furthermore, interacts with the fast bubble flow causing it to move in a wavelike manner

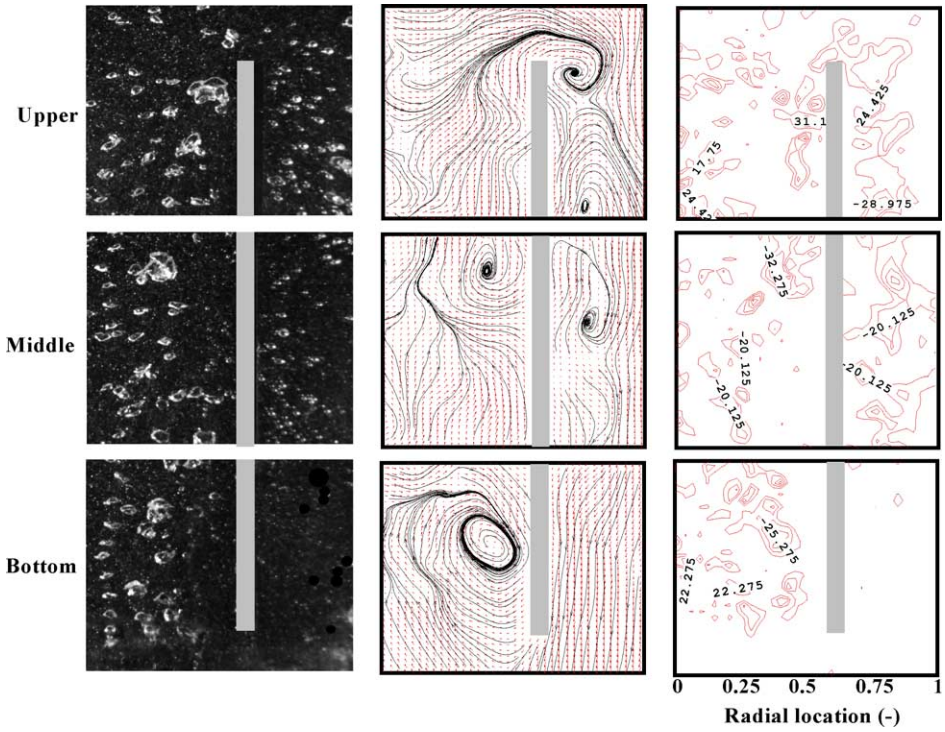

Fig. 4. Instantaneous flow images, streamline and vorticity contours at three sections operating in Regime I with $U_g = 1.43$ cm/s.

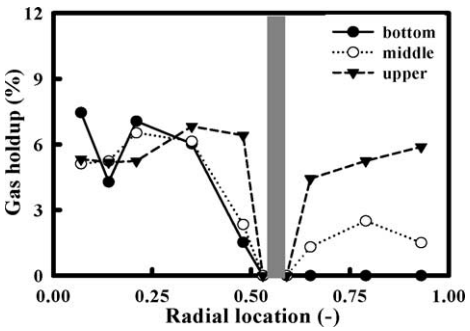

Fig. 5. Gas hold-up distributions at three sections operating in Regime I with U_g = 1.43 cm/s.

as mentioned previously. Although most bubbles are induced away from the sidewalls of the riser, some small bubbles are still trapped within the vortical and descending flows through the interaction between the vortices and fast bubble flow region. Hence, the gas hold-up near the sidewalls in the middle region is a little higher than that in the bottom. These trapped small bubbles in the vortical flow lead to a decrease in local density, thus causing the structures of the vortical flow to ascend or disappear, as demonstrated by three consecutive images in Fig. 6. Another possible cause of the weaker vortical flow is that most of the drifting liquid is recycled to the downcomer and only a small portion of the liquid becomes the descending flow to interact with fast bubble flow. Devanathan et al. [33] from a 3D simulation of the flow in a bubble column has obtained a similar result. However, in the reports of Lin et al. [27], the vortical structures only move downward in 2D bubble columns. With a strong circulation into the downcomer at the upper region, the fast bubble flow is dragged to the sidewalls of the riser to cause a higher gas hold-up, as shown in Fig. 5.

After gas–liquid disengagement, the recycled flow from the riser provides an angular momentum to drag the vortex at the entrance of the downcomer downwards, as shown in Fig. 4. At the same time, some small bubbles are entrained into the downcomer by the recycled flow. These entrained bubbles initially follow the path of the recycled flow, being pushed away from the draft tube by the vortex. This is why a higher value of gas hold-up is shown near the sidewalls of the downcomer, as shown in Fig. 5. Since the downward velocity of the recycled flow is gradually subsided by the wall effect, the entrained bubbles eventually reach a specific depth where the drag force and buoyant force are equal. The entrained bubbles at this depth are easily trapped within the vortex, and then move upwards, leading to the breakage of the structure of the vortex, as shown in Fig. 6. As a result, the gas hold-up in the downcomer gradually decreases with flow downwards. Seigel et al. [17] have also reported this phenomenon. Hence, from the radial distribution of the time-averaged component velocities of the entrained bubbles at the middle section of the downcomer, Fig. 7 shows that the entrained bubbles undergo negative vertical velocities near the sidewall of the reactor but positive vertical velocities near the draft tube. Further downwards, Figs. 4 and 5 show that no bubbles are dragged below the middle section of the downcomer. Since there are

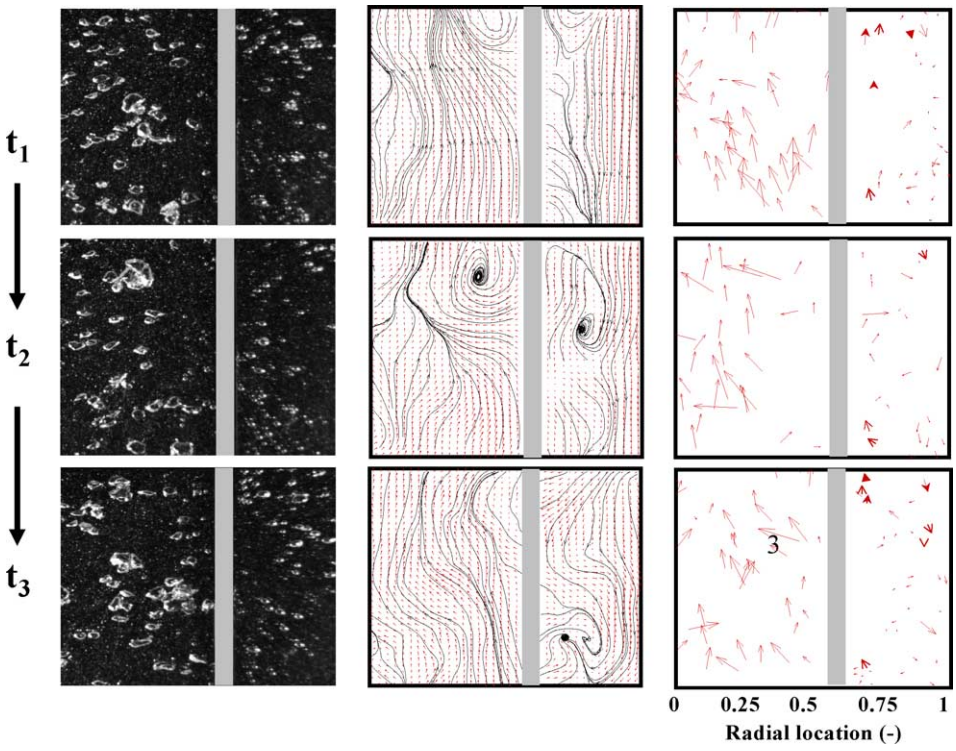

Fig. 6. Three consecutive flow images, streamline, and bubble velocity vector distributions at the middle section in Regime I with U_g = 1.43 cm/s.

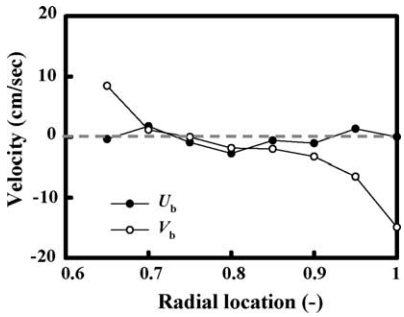

Fig. 7. Radial distribution of the averaged component velocities of the entrained bubbles at the middle section of the downcomer in Regime I with U_g = 1.43 cm/s.

no bubbles and no vortex interruptions, the recycled flow gradually expands and becomes quite uniform at the bottom section of the downcomer.

The time-averaged streamline, component velocity and various Reynolds stress distributions for three sections operated at U_g = 1.43 cm/s are shown in Fig. 8. The main difference between the instantaneous and time-averaged streamlines is the disappearance of the vortical flow in the riser and the downcomer. Because of the cancellation of the swinging motion of the radial velocity after time-averaged integration, the flow character of the wavelike motion is smoothed out and becomes a straight liquid flow in the riser and downcomer. Some fluctuations in the downcomer might occur as a result of insufficient data points at that area for time average. However, a pair of vortices remains located at the entrance of the riser and downcomer, as observed in the instantaneous structure. Taking the time average, the radial liquid velocity shows a zero value both in the riser and downcomer. The axial liquid velocity, induced by bubble wakes and bubble carriage motions, moves uniformly upward in the central plume region. As the liquid is carried upward in the riser by the large bubbles in the fast bubble flow region, the axial velocity increases to a maximum of 15 cm/s. After that, the axial velocity decreases sharply with radial direction and becomes zero (generally called inversion point) at around 90% of the riser half width. According to the studies of Lin et al. [27] and Hills [34], the inversion point in bubble columns is at the location between 60 and 70% of the column half width. Due to a small portion of the driven liquid falling back to the rise, the strength and the occupied area of the descending liquid flow and the vortical flow in the riser are weaker and smaller than those in the bubble column. Suppressed by the vortex at the entrance of the downcomer, the time-averaged vertical velocity initially is a parabolic distribution and progressively develops to a uniform distribution.

Due to bubble movement, two high peaks of $\langle V'V' \rangle$ are found adjacent to the places between the vortex and recycled flow at the entrances of the riser and the downcomer, respectively. It is found that under the same gas velocity, the vortical structures are rather weak in comparison with those in the bubble columns; hence, the normal stresses in the riser do not have the pronounced peaks as previously observed in the bubble columns by Mudde et al. [28]. Instead, the profiles of $\langle U'U' \rangle$ and $\langle V'V' \rangle$ are fairly flat in the riser. In addition, the magnitude of normal stresses (about 60 cm^2/s^2) reported in this study is smaller than that (about 150 cm^2/s^2) in the bubble column reported by Mudde et al. [28] at the same operating conditions. This characteristic suggests that an airlift reactor is more suitably employed in a living cell system than in a bubble column.

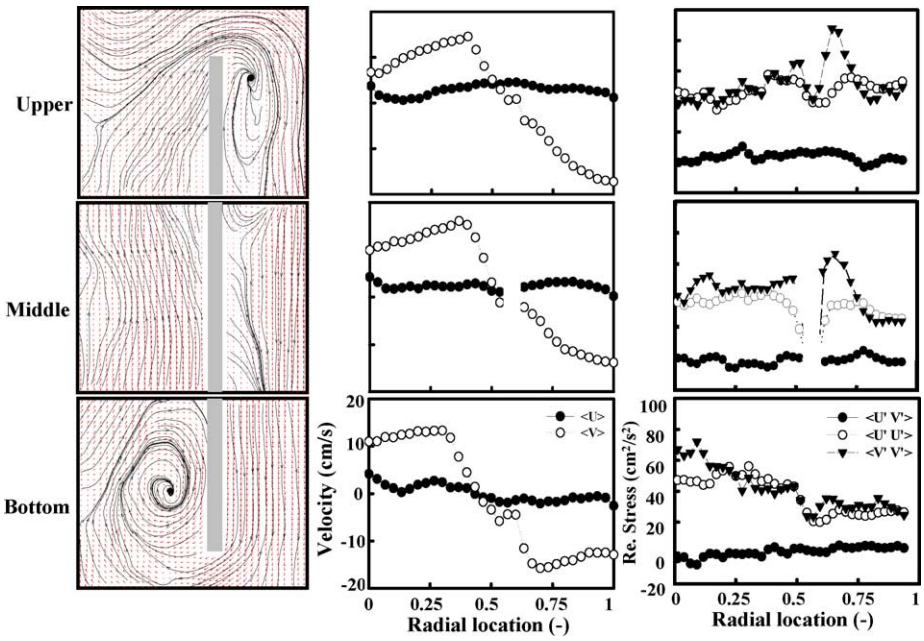

Fig. 8. Averages of streamline contour, component velocity and various Reynolds stress distributions at three sections in Regime I with U_g = 1.43 cm/s.

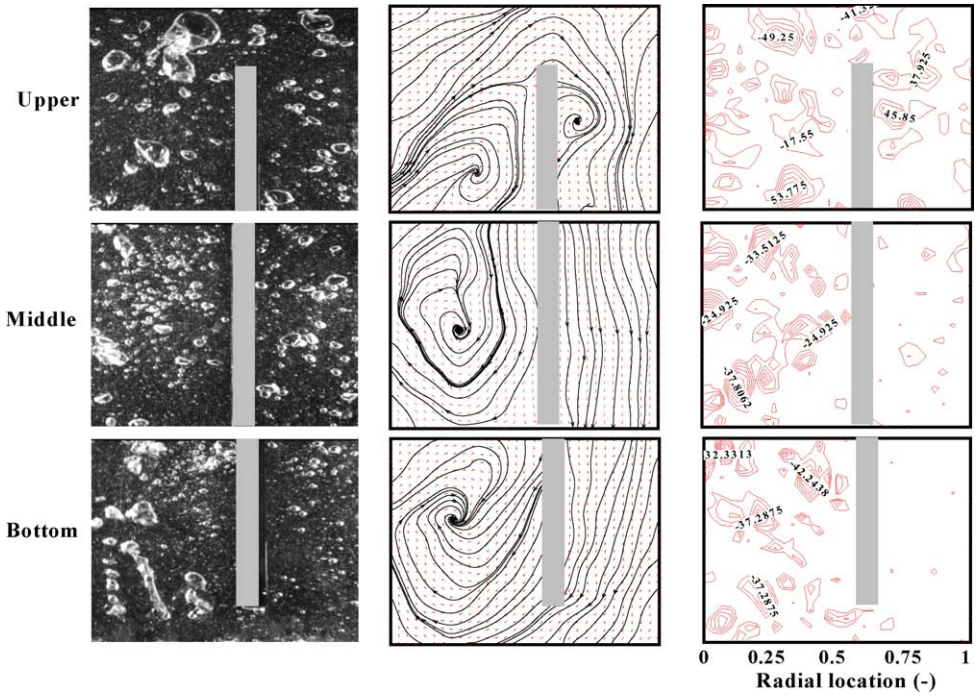

Fig. 9. Instantaneous flow images, streamline and vorticity contours at three sections operating in Regime II with U_g = 3 cm/s.

On the other hand, the vortical structures in the downcomer are considerably stronger, although they may subside after descending to specific depth. The flow in this vortical flow region dynamically changes from downward to upward and experiences large fluctuations in the vertical component of the liquid velocity, leading $\langle V'V' \rangle$ to peak close to the wall of the draft tube in the downcomer. However, because the descending vortices are against the wall of the draft tube, no swinging motion is induced, and this leads to a flat profile on $\langle U'U' \rangle$. Without disturbance from the flow further developing at the bottom section of the downcomer, the normal stresses, $\langle U'U' \rangle$ and $\langle V'V' \rangle$, have a quite even and smaller profile.

3.2.2. Regime II

Increasing the gas velocity to U_g = 3 cm/s, the flow regime transits from Regime I to Regime II, where the two fast bubble flows merge together to form one central fast bubble flow in the center of the riser, as shown in Fig. 9. This central fast bubble flow has caused a uniform gas hold-up distribution at the center of the riser for all three regions, as demonstrated in Fig. 10. Drifting by this central fast bubbleflow, the flow regime is characterized by a global circulation of the liquid phase, wherein the liquid rises in the middle portion of the riser, and descends to the downcomer and the sidewall of the riser. Unlike Regime I, the descending flow adjacent to the sidewall of the riser is strong enough to encounter the central fast bubble flow, and yields a consecutive descending vortical flow. This descending vortical flow consists of multiple vortices, which are staggered and descending along the sidewalls of the riser without breakage by the trapped bubbles. From the distribution of vorticity in this figure, high vorticity is usually produced at the two sides of the boundaries of the vortical flow, where high shear rates are continuously supplied through the opposite velocities between these coherent flows.

It is observed that some of the large bubbles break into small bubbles because of the high turbulent intensity induced by the buoyancy force and the recycled liquid velocity. Eventually, the large bubbles escape from the liquid surface and the rest of the bubbles are entrained by the recycled flow to the downcomer. Continuously descending, the recycled flow further interacts with the entrained bubbles and causes bubble coalescence and elevation, which leads to a reduction of the strength of the recycled flow. Finally, only small bubbles can be entrained and circulated back to the riser. As a result, the gas hold-up gradually decreases with descent downwards in the downcomer, as shown in Fig. 10. Because of

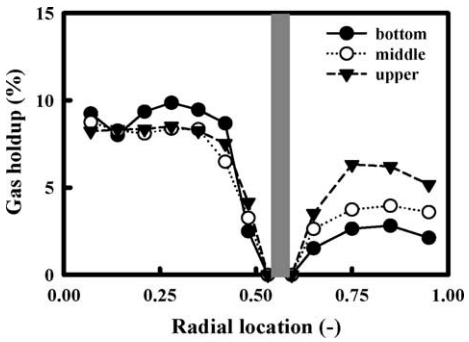

Fig. 10. Gas hold-up distributions at three sections operating in Regime II with U_g = 3 cm/s.

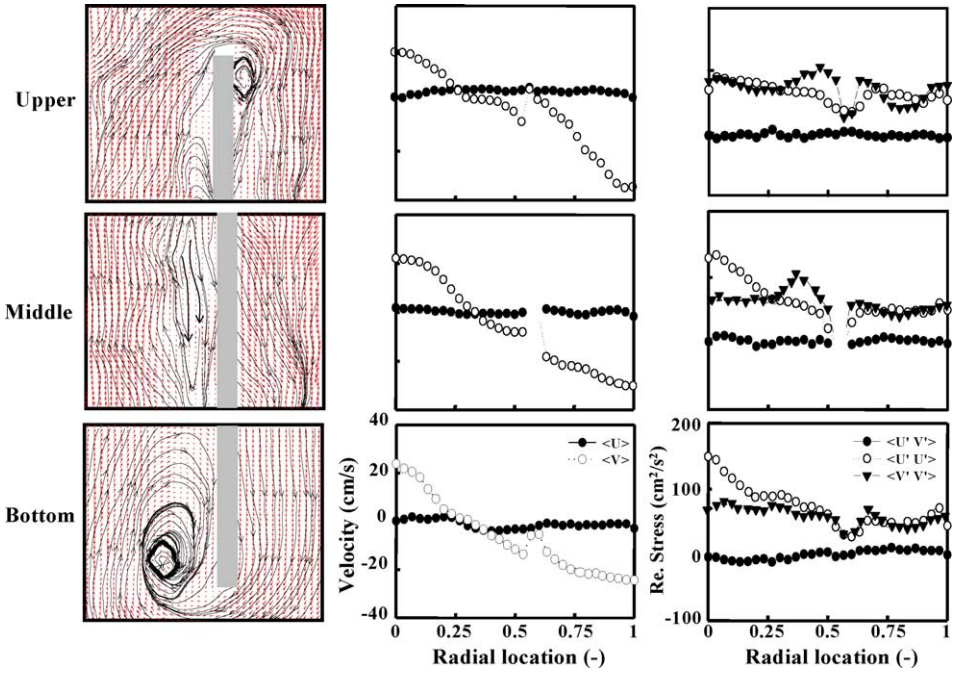

Fig. 11. Averages of streamline contour, component velocity and various Reynolds stress distributions at three sections in Regime II with $U_g = 3$ cm/s.

intense strength and large volume, the recycled flow nearly overwhelms the entrance of the downcomer and suppresses the vortex at the entrance of the downcomer to a confined size, but without being dragged downward. Consequently, a high vorticity is generated at the place between the vortex and the recycled flow. Due to the absence of disruption of the descending vortex, no large vorticity occurs at the middle of the downcomer, even though the dragged bubbles may induce some fluctuations. This phenomenon reveals a significant difference from that in Regime I.

Fig. 11 shows the time-averaged streamline, component velocity and various Reynolds stress distributions for three sections operated at $U_g = 3$ cm/s. Similar to Regime I, this regime shows that the coherent structure of the vortical flow was cancelled out and only two vortices reside at the entrances of the riser and downcomer, respectively. The magnitudes of velocities and Reynolds stresses in Regime II are the largest among all three regimes. In the riser, the time-averaged radial velocities are negligibly small at the bottom and middle sections. While at the upper section, the time-averaged radial velocity appears to be positive, because the captured view taken here is the lower part of upper section, which contains a positive recycled flow. The distributions of the time-averaged axial velocities for all sections are positive in the center and negative near the sidewall, which are similar to the typical gross scale circulation previously reported in bubble columns by numerous researchers [34–36]. The inverse point is located at about 70% of the riser half width, which has the same position as the bubble columns. The maximal axial velocity is about 20 cm/s located at the riser center, where the central bubble stream occupies. In the downcomer, an inclined distribution for the averaged axial velocity is obtained for all three sections. However, the inclined slope is gradually decreases as the flow progresses to the bottom of the downcomer.

In the riser, the magnitude of the normal stresses is almost two orders larger than that of the shear stresses. In the middle section of the riser, the maximums of the $\langle U'U' \rangle$ and $\langle V'V' \rangle$ are located at the center and close to the wall, respectively. The nature of the normal stresses is evident by considering the swinging motion of the central fast bubble flow. In the center of the riser, although the fast bubble flow is more frequently upward, the swinging motion of the flow leads to peaking in $\langle U'U' \rangle$ since the axial velocity attains its highest magnitude in the center. While the vortical flow experiences large fluctuations in the vertical component of the liquid velocity, leading $\langle V'V' \rangle$ to peak closer to the wall of the riser than in the center, where the motion is primarily directed upward. However, because the vortex at the entrance of the riser is steady with rather uniform downflow or upflow, no significant radial fluctuation is contributed to $\langle V'V' \rangle$. In the upper section, violent degassing causes a fluctuation in the vertical direction and results in a higher value in $\langle V'V' \rangle$. In the downcomer, the axial liquid velocity is irritated by the recycled flows to induce a high value in $\langle V'V' \rangle$ at the entrance and exit regions. Without the fluctuation of the descending vortex, there is no significant peak for the distributions of the normal and shear stresses at the middle section of the downcomer.

4. Concluding remarks

Our quantitative analysis based on data obtained using the PIA technique, provides insight into the instantaneous and

time-averaged flow behaviors in a gas entrainment regime for a two-dimensional internal-loop airlift reactor. Two subregimes (Regimes I and II) can be demarcated based on the re-circulation of bubbles back to the riser. For both regimes, the instantaneous wave-like motion generated by fast bubble flow in the riser is evened out, and results in an upward motion after taking the time average. In Regime I, because of decreasing the local density by trapping small bubbles in the vortical flow and recycling only a small portion of the liquid back to the riser, the flow conditions in the riser yield a weaker vortical flow, a less significant change in normal stresses, and the inversion point shifts to a location 90% of the riser half width. With a balance of the drag force and the buoyant force, the dragged bubbles in the downcomer reach a specific depth, and then move upward to interact with the vortex. For Regime II, the existence of the central fast bubble flow results in a parabolic profile of the vertical velocity with a maximal value at the center and an inverse point at 70% diameter of the riser. The normal stresses are two orders of magnitude larger than the shear stress, including a maximum of $\langle U'U' \rangle$ at the center of the riser due to the swing of the fast bubble flow, and a maximum of $\langle V'V' \rangle$ close to the wall due to the vertical fluctuation of the vortical flow. The bubbles entrained into the downcomer can interact with the recycled flow and level out the inclined velocity profile.

Acknowledgement

The work was supported by a National Science Council grant NSC-92-2214-E- 194-007 in The Republic of China.

References

[1] Y. Chisti, Airlift Bioreactor, Elsevier Applied Science, London, 1989.
[2] L.-S. Fan, Gas–Liquid–Solid Fluidization Engineering, Butterworths, Stoneham, 1989.
[3] J.J. Heijnen, A. Mulder, R. Weltevrede, J. Hols, H.L.J.M. van Leeuwen, Large scale anaerobic-aerobic treatment of complex industrial waste water using biofilm reactors, Water Sci. Technol. 23 (1991) 1427–1436.
[4] M.Y. Chisti, M. Moo-Young, Disruption of microbial cells for intracellular products, Enzyme Micro. Technol. 8 (1986) 194–204.
[5] M.Y. Chisti, B. Halrd, M. Moo-Young, Liquid circulation in airlift reactors, Chem. Eng. Sci. 43 (1988) 451–457.
[6] S. Royse, Scaling Up for Mammalian Cell Culture, The Chemical Engineer, November 12, 1987.
[7] J.E. Bailey, Biochemical reaction engineering and biochemical reactors, Chem. Eng. Sci. 35 (1980) 1854–1886.
[8] K. Koide, S. Iwamoto, Y. Takasaka, S. Matsuura, E. Takahashi, M. Kimura, Liquid circulation, gas holdup and pressure drop in bubble column with draught tube, J. Chem. Eng. Jpn. 17 (1984) 611–618.
[9] P. Weiland, Influence of draft tube diameter on operation behavior of airlift loop reactors, German Chem. Eng. 7 (1984) 374–385.
[10] D.A. Sanders, C. Howard, A.D. Hudson, Modeling of the fluid dynamics processes in a high-recirculation airlift reactor, Int. J. Energy Res. 25 (2001) 487–500.
[11] M.Y. Chisti, M. Moo-Young, Airlift reactors: characteristics, applications and design considerations, Chem. Eng. Commun. 60 (1987) 195–242.
[12] P. Weiland, U. Onken, Differences in the bubble columns and airlift loop reactors, German Chem. Eng. 4 (1981) 174–181.
[13] J.C. Merchuk, Gas holdup and liquid velocity in a two dimensional airlift reactor, Chem. Eng. Sci. 41 (1986) 11–16.
[14] J.J. Heijnen, J. Hols, R.G.M. van der Lans, H.L.J.M. van Leeuwen, A. Mulder, R. Weltevrede, A simple hydrodynamic model for the liquid circulation velocity in full scale three phase airlift reactor, Chem. Eng. Sci. 52 (1997) 2527–2540.
[15] Van Benthum, W.R. Van der Lans, M. Van Loosdrecht, J. Heijnen, Bubble recirculation regimes in an internal-loop airlift reactor, Chem. Eng. Sci. 54 (1999) 3995–4006.
[16] W. Freedman, J.F. Davidson, Holdup and liquid circulation in bubble columns, Trans. Inst. Chem. Eng. 47 (1969) 251–260.
[17] M.H. Siegel, J.C. Merchuk, K. Schugerl, Airlift reactor analysis: interrelationships between riser, downcomer, and gas–liquid separator behavior, including gas recirculation effects, AIChE J. 32 (1986) 1585–1596.
[18] Y. Kawase, M. Moo-Young, Mixing and mass transfer in concentric-tube airlift fermenters: Newtonian and non-Newtonian media, J. Chem. Technol. 36 (1986) 527–533.
[19] Z. Kemblowski, J. Przywarski, A. Diab, An average gas hold-up and liquid circulation velocity in airlift reactors with external loop, Chem. Eng. Sci. 48 (1993) 4023–4035.
[20] Y. Hsu, M.P. Dudukovic, Gas holdup and liquid recirculation in gas-lift reactors, Chem. Eng. Sci. 35 (1980) 135–141.
[21] P. Verlaan, J. Tampert, K. Van't Riet, K. Luyben, A hydrodynamic model for an airlift-loop bioreactor with external loop, Chem. Eng. J. 33 (1986) 43–53.
[22] C.G. Eloy, P. Letón, Prediction of gas holdup and liquid velocity in airlift reactors using two-phase flow friction coefficients, J. Chem. Technol. Biotechnol. 67 (1996) 388–396.
[23] M.A. Young, R.G. Carbonell, D.F. Ollis, Airlift bioreactors: analysis of local two-phase hydrodynamics, AIChE J. 37 (1991) 403–428.
[24] S. Becker, A. Sokolichin, G. Eigenberger, Gas–liquid flow in bubble columns and loop reactors: part II. Comparison of detailed experiments and flow simulations, Chem. Eng. Sci. 49 (1994) 5747–5762.
[25] M. Utiger, F. Stuber, A.M. Duquenne, H. Delmas, C. Guy, Local measurements for the study of external loop airlift hydrodynamics, Can. J. Chem. Eng. 77 (1999) 375–382.
[26] J. Reese, L.-S. Fan, Transient flow structure in the entrance region of a bubble column using particle image velocimetry, Chem. Eng. Sci. 49 (1994) 5623–5636.
[27] T.-J. Lin, J. Reese, T. Hong, L.-S. Fan, Quantitative analysis and computation of two dimensional bubble columns, AIChE J. 42 (1996) 301–318.
[28] R.F. Mudde, D.J. Lee, J. Reese, L.-S. Fan, Role of coherent structures on Reynolds stresses in a 2-D bubble column, AIChE J. 43 (1997) 913–926.
[29] R.C. Chen, I.S. Chou, Preliminary studies of bubble wake dynamics using particle image analyzer, J. Chin. Soc. Mech. Eng. 19 (1998) 475–485.
[30] K. Tsuchiya, L.-S. Fan, Near-wake structure of a single gas bubble in a two-dimensional liquid–solid fluidized bed: vortex shedding and wake size variation, Chem. Eng. Sci. 43 (1988) 1167–1184.
[31] T. Miyahara, T. Tsuchiya, L.-S. Fan, Wake properties of a single gas bubble in a three-dimensional liquid–solid fluidized bed, Int. J. Multiphase Flow 14 (1988) 749–763.
[32] R.C. Chen, J. Reese, L.-S. Fan, Flow structure in a three-dimensional bubble column and three-phase fluidized bed, AIChE J. 40 (1994) 1093–1104.

[33] N. Devanathan, M.P. Dudukovic, A. Lapin, A. Lubbert, Chaotic flow in bubble column reactors, Chem. Eng. Sci. 50 (1995) 2661–2667.
[34] J.H. Hills, Radial non-uniformity of velocity and voidage in a bubble column, Trans. Inst. Chem. Eng. 52 (1974) 1–9.
[35] K. Franz, T. Borner, H.J. Kantorek, R. Buchholz, Flow structures in bubble columns, German Chem. Eng. 7 (1984) 365–374.
[36] T. Menzel, T. in der Weide, O. Staudacher, O. Wein, U. Onken, Reynolds shear stress for modeling of bubble column reactors, Ind. Eng. Chem. Res. 29 (1990) 988–994.